Impression Creep Characteristics of a Cast Mg Alloy

B. KONDORI and R. MAHMUDI

The creep behavior of the cast Mg-6Al-0.3Mn alloy (AM60) was investigated by impression testing under constant punching stress in the range 150 to 650 MPa and at temperatures in the range 423 to 523 K, corresponding to $0.458 < T/T_m < 0.567$. The creep behavior can be divided into two stress regimes, with a change from the low-stress regime to the high-stress regime occurring, depending on the testing temperature, around $0.021 < (\sigma/G) < 0.033$. Based on the steady-state power-law creep relationship, the stress exponents of 4 to 6 and 8 to 12 were obtained at low and high stresses, respectively. When the experimental creep rates were normalized to the pipe diffusion coefficient, however, the stress exponents of about 5 and 10 were obtained for the low- and high-stress regimes, respectively. The low-stress regime activation energies of about 76 to 84 kJ mol^{-1}, which are close to 80 kJ mol^{-1} for dislocation-pipe diffusion in the Mg, and stress exponents in the range 4 to 6 suggest that the operative creep mechanism is dislocation climb. This behavior is in contrast to the high-stress regime, in which the stress exponents of 8 to 12 and activation energies of about 134 to 165 kJ mol^{-1} are indicative of a power-law breakdown.

I. INTRODUCTION

RECENTLY, magnesium alloys have received increasing attention due to a strong desire for reduction of weight and fuel emission. Magnesium offers a good combination of low density, high strength-to-density ratio, and good corrosion resistance. These properties along with low-cost processing *via* die casting have nominated magnesium as a potential competitor for metals such as aluminum, steel, and polymers in aerospace and automotive applications.[1] However, low mechanical properties at elevated temperatures, especially creep resistance, limit the use of magnesium alloys to applications at low temperatures.[2]

Aluminum, as the most favorable alloying element, improves die castability and mechanical properties of magnesium at room temperature without significantly raising its density. As a result, the most commonly used magnesium alloys are those based on Mg-Al, such as AZ91 and AM60, which have covered about 90 pct of the total magnesium market for structural applications. A part of the added aluminum dissolves into the matrix and improves the mechanical properties of magnesium through solid solution hardening. For aluminum contents higher than 2 wt pct, a new β-Mg$_{17}$Al$_{12}$ phase could form as particles and precipitates, improving room-temperature mechanical properties of the alloys by hindering dislocation movements. Moreover, the Mg$_{17}$Al$_{12}$ phase has a low melting point of about 437 °C, which improves die castability. However, this phase softens readily at high temperatures ($T > 130$ °C),

and thus has deleterious effects on the creep properties of Mg-Al based alloys. Finding a way to suppress this drastic drop in mechanical properties would introduce new applications for these alloys in automotive and aerospace industries. Accordingly, improvement of mechanical properties, especially creep resistance of Mg-Al based alloys, has attracted a substantial amount of research work.

Recent investigations on creep-resistant magnesium alloys have focused on determining deformation mechanisms,[3,4] studying the effects of alloying elements on the high-temperature deformation behavior,[5–9] and developing models for predictive purposes.[10] It has been found that reduction of Al content and formation of intermetallic phases having high thermal stability are effective ways to develop more creep-resistant Mg-Al alloys.[11] Therefore, the AM60 alloy (Mg-6 wt pct Al-0.3 wt pct Mn) with a lower Al content than the most commonly used AZ91 magnesium alloy offers acceptable room-temperature mechanical properties that can be considered as a suitable candidate for further studies on creep-resistant magnesium alloys. Despite a great number of investigations on magnesium alloys and their properties, there are limited data on high-temperature properties, especially creep performance of the AM60 alloy. Blum *et al.*[12] have carried out a comparative study on creep of several magnesium alloys including AM60 alloy. Ishimatsu *et al.*[13] investigated the creep properties of AM50 alloy (Mg-5 wt pct Al-0.3 wt pct Mn), an alloy with a composition close to AM60, in the temperature range 423 to 498 K. Depending on the applied stress levels, they discerned two distinct creep regimes. The low-stress regime with $n = 5$ and $Q = 121 \pm 10$ kJ/mole was attributed to the dislocation climb mechanism. The higher values of $n = 12$ and $Q = 162$ kJ/mole in the high-stress regime, however, were ascribed to the instantaneous plastic strain caused

B. KONDORI, Graduate Student, and R. MAHMUDI, Professor, are with the School of Metallurgical and Materials Engineering, University of Tehran, Tehran, Iran. Contact e-mail: mahmudi@ut.ac.ir

by the applied load that could induce many dislocations and cause higher creep rates.

The impression creep test, developed by Chu and Li,[14] is a unique method for determining creep behavior of different materials. This technique is a modified version of the indentation creep method, in which a flat bottomed cylindrical punch is pushed into the test specimen under a constant load and the impression depth is recorded during dwell time. In contrast to the conventional creep tests, which need tensile or compressive specimens, in this method, all creep data can be obtained with a small piece of material. Recently, localized creep test methods have been used to evaluate creep behavior of different magnesium alloys. The creep behavior of magnesium alloys has mostly been investigated by indentation tests using spherical indenters[15–17] and, in a few cases, by impression techniques.[18,19] The impression creep of AM60 alloy has not been studied previously, and thus, the aim of this study is to investigate creep properties of this alloy using the impression testing technique.

II. EXPERIMENTAL PROCEDURE

The material used was an AM60 alloy with a nominal chemical composition of Mg-6 wt pct Al-0.3 wt pct Mn. It was prepared from high-purity (99.8 pct) magnesium, aluminum, and manganese, melted in a graphite crucible placed in an electrical resistance furnace under the protective MAGREX 36* flux cover. After melting

---

*MAGREX 36 is a trade mark of Foseco, Staffordshire, United Kingdom.

---

magnesium at 1023 K, aluminum and manganese were added as alloying elements. The melt was held at this temperature for 30 minutes and then stirred mechanically for 2 minutes using a stainless steel rod to provide a homogeneous composition. The melt was held at 1023 K for another 10 minutes to ensure settlement of oxide particles and other contaminants. It was then poured into a mild steel mold preheated to 573 K, using a tilt-casting system to minimize the melt turbulence. Casting bars had dimensions of $12 \times 30 \times 200$ mm, from which $4 \times 12 \times 30$ mm slices were cut by an electrodischarge wire-cut machine for impression creep testing and structural characterization.

Cast samples were studied by scanning electron microscopy (SEM) to examine the as-cast microstructure as well as the evolution of microstructure after creep. The specimens were polished with 0.3-μm alumina powder and distilled water. Etching was carried out using an acetic picric etchant at room temperature. X-ray diffraction (XRD) analysis was carried out on selected specimens to identify the existing phases. Energy dispersive spectroscopy (EDS) analysis was performed to reveal Al concentration in different areas of the microstructure. Some specimens after creep were cut parallel to the loading direction in order to study the microstructure evolution in the deformation zone beneath the indenter.

Impression creep tests were carried out in an MTS universal testing machine equipped with a three-zone split furnace to perform constant-load impression tests in the air atmosphere. A flat ended cylindrical punch of 2-mm diameter was mounted in a holder, which was positioned in the center of the vertical loading bar. The specimen was located on an anvil below the loading bar, and the assembly of the specimen and indenter was accommodated by the split furnace. The tests were performed in the temperature range 423 to 523 K, corresponding to $0.458 < T/T_m < 0.567$, and under applied stresses in the range 150 to 650 MPa for dwell times of up to 3600 seconds. After application of the load, the impression depth was measured automatically as a function of time by the machine and the data were acquired by a computer. The accuracy of testing temperature control was within ± 0.2 K, while test specimens were loaded with an accuracy of ± 1 N and impression depth recording resolution of 1 μm.

III. RESULTS

The SEM micrograph of the alloy, shown in Figure 1(a), is indicative of a dendritic microstructure with some second-phase particles distributed in the interdendritic regions. X-ray diffraction analysis presented in Figure 1(b) reveals that α-Mg and β-$Mg_{17}Al_{12}$ intermetallic compounds are the only constituents of the as-cast microstructure. The SEM micrograph of the alloy at higher magnification is depicted in Figure 2(a). This picture shows α-Mg dendrites (labeled as A) that are surrounded by dark regions (marked as B). Figure 2(b) shows the EDS analysis of this dark region at the vicinity of dendrites and compares it with the results obtained from α-Mg dendrite's core. The quantitative analysis reveals that the Al content of this supersaturated region (9.10 pct) is 2 or 3 times higher than that of the α-Mg dendrites (4.11 pct). In addition to the α-Mg dendrites, there exist some β-$Mg_{17}Al_{12}$ intermetallics with two different morphologies, which are mainly located in the interdendritic regions. A major portion of this phase is in the form of bulky particles with irregular morphology that is marked as C in Figure 2(a). In the vicinity of these bulky particles, however, there are some fine lamellar precipitates known as discontinuous $Mg_{17}Al_{12}$ precipitates, marked as D.

The impression creep test was carried out at different temperatures ranging form 423 to 523 K under different applied stresses. Figure 3 represents typical impression creep curves expressed as impression depth *vs* dwell time at 423 K under stress levels in the range 400 to 650 MPa. Similarly, the creep of the material can be compared at different temperatures under a constant stress, as shown for $\sigma = 400$ MPa in Figure 4. As can be seen, in both cases, after a rather short primary creep stage, the curves show a relatively long steady-state region where depth increases linearly with time. Furthermore, it is obvious that with increasing the applied stress at a constant temperature or with increasing the temperature under a given stress level, the steady-state region occurs at shorter periods of time and
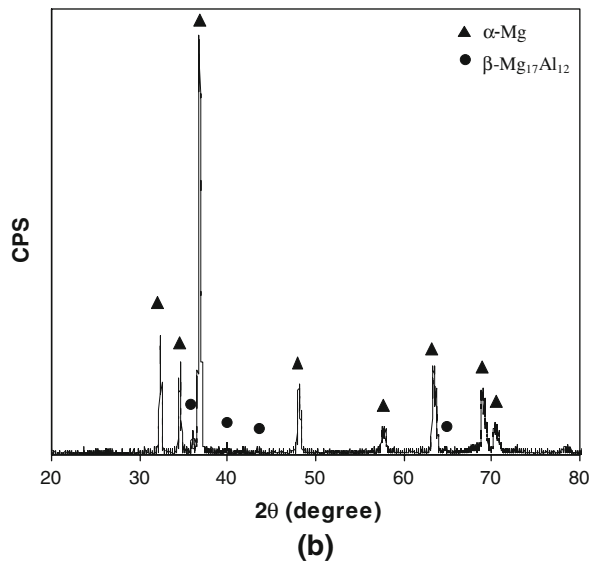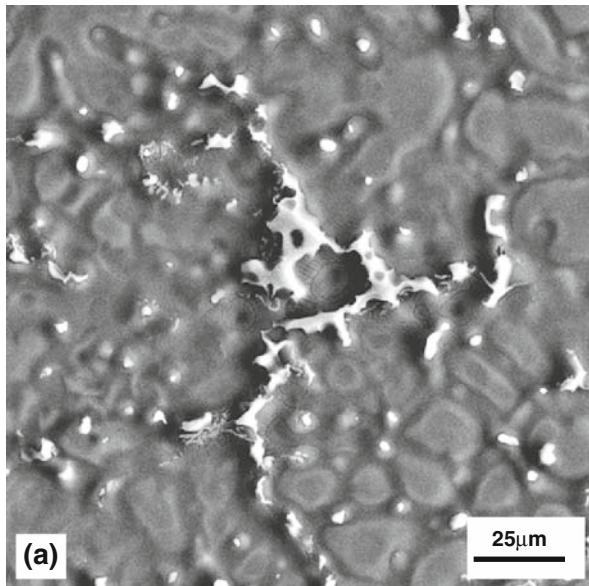
Fig. 1—(*a*) SEM micrograph of the cast material and (*b*) the corresponding XRD pattern, showing α-Mg and β-Mg$_{17}$Al$_{12}$ phases.

Fig. 2—(*a*) SEM micrograph showing A: α-Mg dendrite, B: supersaturated α-Mg, C: β-Mg$_{17}$Al$_{12}$ particles, and D: discontinuous β-Mg$_{17}$Al$_{12}$ precipitates; and (*b*) EDS analyses of regions A and B.

creep occurs more readily. By differentiating impression creep data, one can plot the steady-state impression rate ($V = dh/dt$) against impression depth. The data obtained by differentiating creep curves are used in plotting the impression rate as a function of stress and impression depth, shown, respectively, in Figures 5(a) and (b).

It is generally accepted that the mechanical behavior of metallic materials at homologous temperatures higher than 0.5 can be fairly expressed by the power-law creep over a wide range of strain rates. Thus, for steady-state creep, the high-temperature creep rate $\dot{\varepsilon}$ is often described by the well-known Dorn equation:[20]

$$\dot{\varepsilon} = A\left(\frac{GbD}{kT}\right)\left(\frac{\sigma}{G}\right)^n \exp\left(-\frac{Q}{RT}\right) \qquad [1]$$

where A is a material parameter, **b** the Burgers vector, G the shear modulus, D the diffusion coefficient, k the
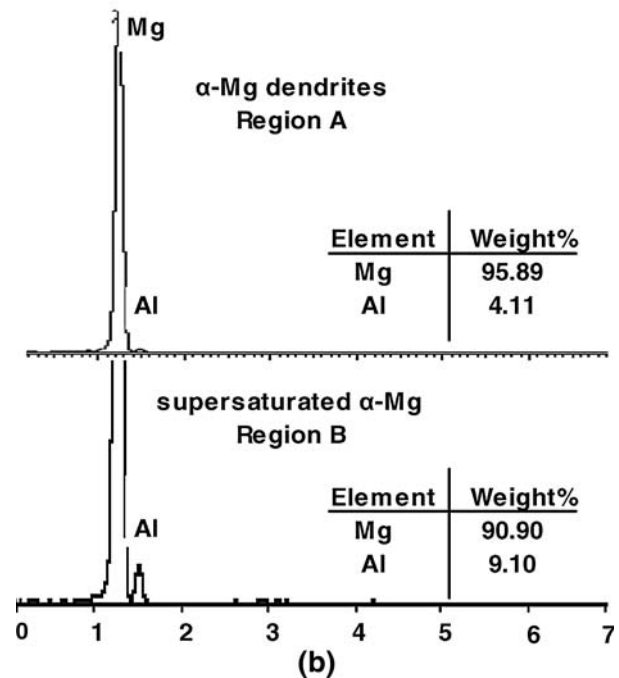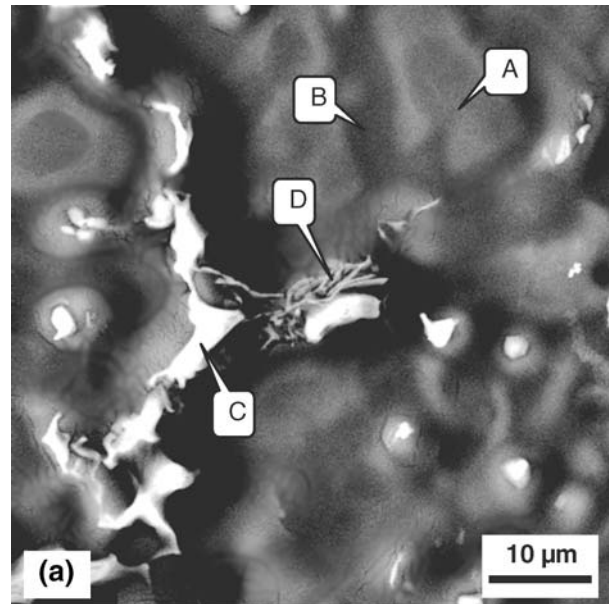
Boltzmann's constant, T the temperature, σ the applied stress, n the stress exponent, Q the creep-activation energy, and R the universal gas constant.

To correlate the impression and tensile creep data, the equivalent stress and strain rate can be evaluated from the impression velocity ($V = dh/dt$), the impression stress under the punch ($\sigma = 4F/\pi\phi^2$) at a given load F and punch diameter ϕ as

$$\sigma = \frac{\sigma_{imp}}{c_1} \text{ and } \dot{\varepsilon} = \frac{dh/dt}{\phi c_2} = \frac{V_{imp}}{\phi c_2} \qquad [2]$$
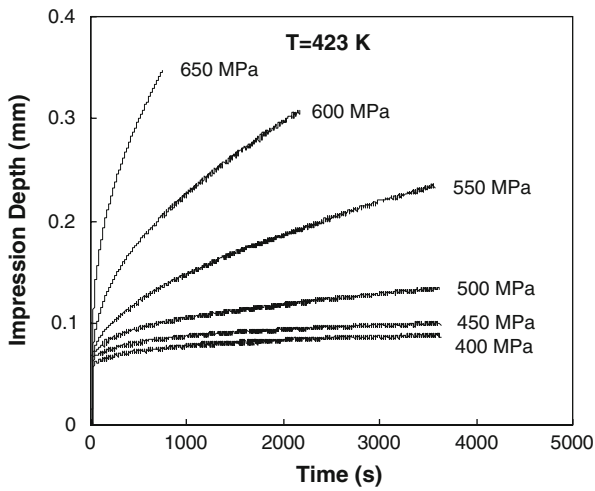
Fig. 3—Impression creep curves expressed as impression depth against dwell time obtained at $T = 423$ K.
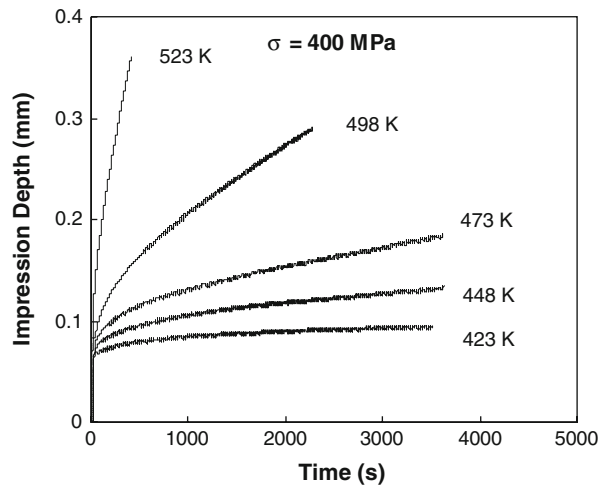

Fig. 4—Impression creep curves obtained at different temperatures and $\sigma = 400$ MPa.
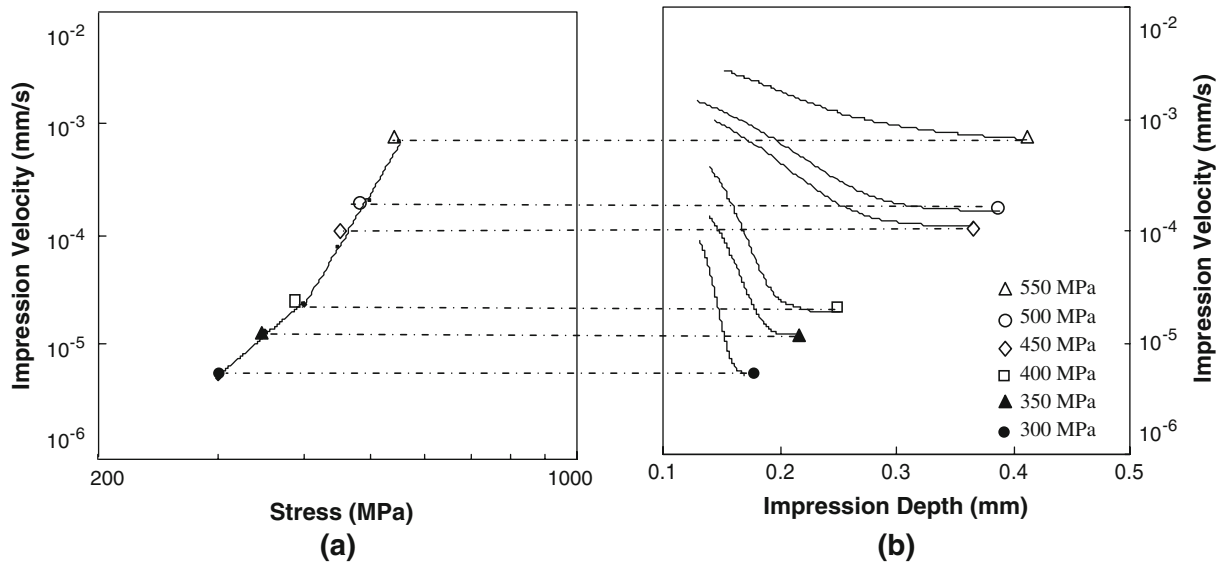

Fig. 5—(a) Impression velocity as a function of punch stress and (b) the same variable plotted against time at $T = 423$ K for different stress levels. Indicated points represent steady-state creep rate at each stress.

where c_1 and c_2 are constants. It has been shown experimentally that both stress and temperature dependencies of the steady-state impression velocity agree with the corresponding dependencies of the creep rate in conventional creep tests.[14,21,22] Therefore, inserting Eq. [2] into Eq. [1] and rearranging gives the relationship between the impression velocity and the applied punch stress. Accordingly,

$$\left(\frac{VT}{G}\right) = B\left(\frac{\mathbf{b}D}{\mathrm{k}}\right)\left(\frac{\sigma}{G}\right)^n \exp\left(-\frac{Q}{\mathrm{R}T}\right) \qquad [3]$$

where B is a material parameter. Since $\mathbf{b}$ and k are constants, it is possible to obtain the stress exponent n from a plot of $\ln(VT/G)$ against $\ln(VT/G)$ at constant T. Similarly, the activation energy Q can be obtained from a plot of $\ln(VT/G)$ vs $(1/T)$ at constant (σ/G). It should

be noted that shear modulus is a function of testing temperature, and thus, the corresponding relationship should be considered in the calculation of n and Q values. For the present material, the temperature dependence of the shear modulus was calculated from the following equation:[23]

$$G(\mathrm{MPa}) = 18,460 - 8.2T\,(\mathrm{K}) \qquad [4]$$

According to Eq. [3], if the normalized impression velocity is plotted against normalized stress on a log-log scale, a line with slope n can be obtained. This has been shown in Figure 6, where there are two distinct regimes with different slopes at low and high stresses. Moreover, the stress exponent decreases from 6 to 4 in the low-stress regime (I) and from 12 to 8 in the high-stress regime (II) as temperature increases from 423 to 523 K.
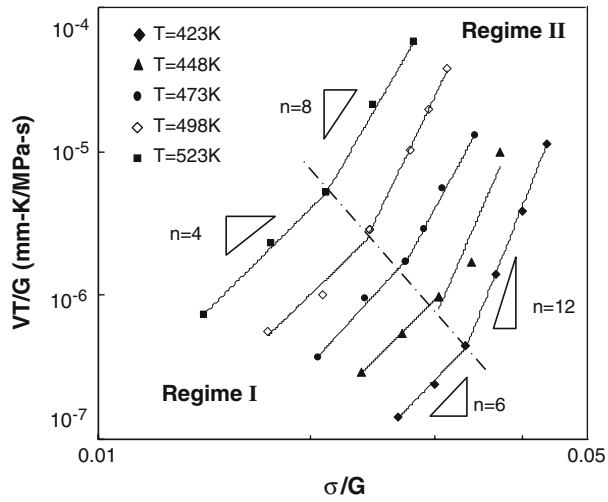
Fig. 6—Normalized steady-state velocity as a function of normalized punching stress at different temperatures for determining n values. Two stress regimes are discernible.
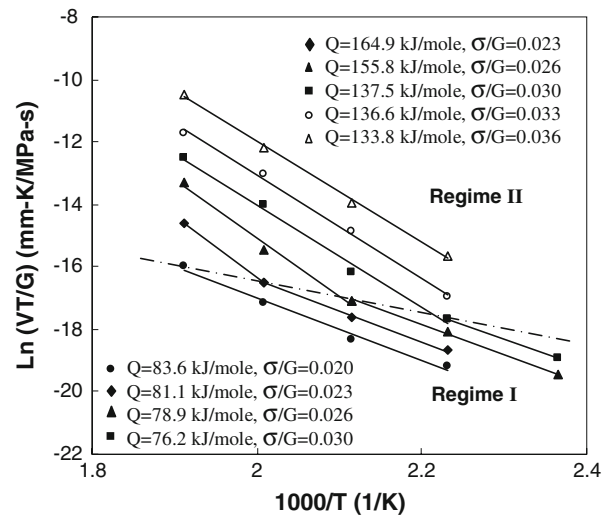

Fig. 8—Temperature dependence of the normalized steady-state impression velocity at different constant normalized punching stresses for determining Q values in the stress regimes I and II.
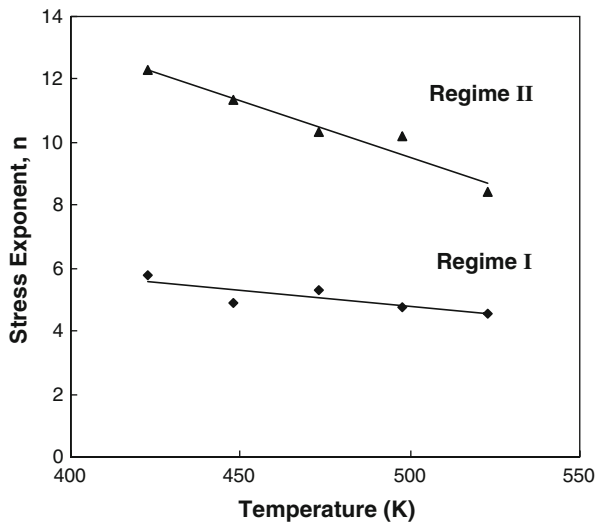

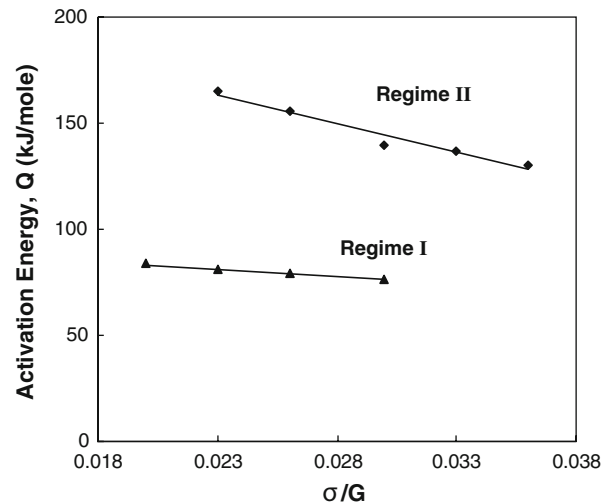Fig. 7—Temperature dependence of the stress exponent in the stress regimes I and II.

Fig. 9—Stress dependence of creep activation energy in the stress regimes I and II.

The temperature-dependence of the stress exponent is plotted for both low- and high-stress regimes in Figure 7. In both regimes, the stress exponent decreases with increasing temperature, the effect of which is more pronounced in the high-stress regime. In order to obtain the activation energy values, the normalized steady-state impression velocities, VT/G, were plotted against the reciprocal of the absolute temperature on a semilogarithmic scale, as shown in Figure 8. Analogous to the curves in Figure 6, an abrupt change in the values of activation energy is evident, indicating a change in the rate controlling mechanisms. The activation energies, calculated from the slopes of the curves $(-Q/R)$, show a decrease from about 165 to 134 kJ/mol in the high-stress regime, and from about 84 to 76 kJ/mol in the low-stress regime, as σ/G increases. The stress dependence of creep

activation energy is shown in Figure 9. It can be observed that in both regimes, the creep activation energy decreases with increasing stress, the effect being less pronounced for the low-stress regime I.

To study the microstructure evolution of the material during impression creep, some crept samples were sectioned along the impression direction in the middle of the impressed area and the microstructure was studied beneath the indenter. Figure 10(a) illustrates the microstructure evolution in the vicinity of the edge of impression after creep testing at 448 K. As can be observed, there are three distinguishable regions separated from each other by curved lines. No microstructural changes are detectable in the dead zone region immediately below the indenter that is not deformed during creep test. Adjacent to this zone, there exists a
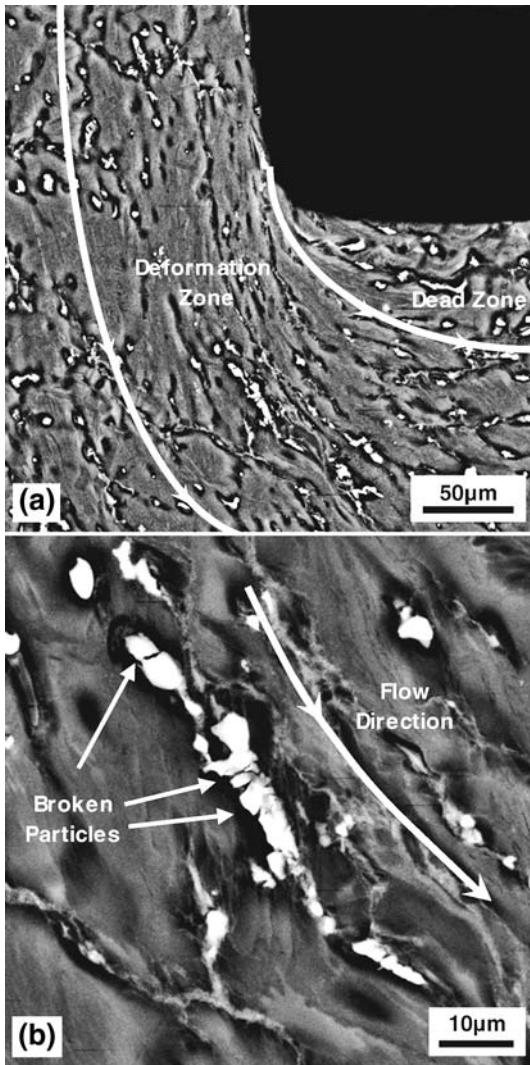
Fig. 10—(a) Cross section of the impression edge at 448 K and $\sigma = 450$ MPa, where the deformation zone is shown by arrows; and (b) a higher-magnification view of the broken and strained particles along flow direction in the deformation zone.

severely deformed region, in which the strained and broken β-$Mg_{17}Al_{12}$ particles are aligned in the direction of material flow, as marked with curved arrows. These particles, which trace the direction of deformation, are shown in Figure 10(b) at a higher magnification. From this picture, one can easily see how β-$Mg_{17}Al_{12}$ particles are strained along the deformation path and are broken as a result of severe plastic deformation. Far from the indenter, the material experiences almost no deformation and the distribution of second-phase particles is not affected by deformation.

IV. DISCUSSION

A. Microstructural Observations

The microstructure of the AM60 alloy, shown in Figure 1(a), consists of α-Mg dendrites and β-$Mg_{17}Al_{12}$ particles, mainly located in interdendritic areas.

These intermetallics, which are usually observed in the microstructure of cast Mg-Al alloys with aluminum contents higher than 2 wt pct, are produced by a eutectic reaction at 710 K. The β-$Mg_{17}Al_{12}$ particles have an irregular bulky morphology, surrounded by aluminum-supersaturated regions. The high cooling rates of molten magnesium during solidification in steel molds lead to the entrapment of aluminum atoms in the magnesium matrix and to the formation of these supersaturated domains, as displayed in Figure 2(a). After solidification and during cooling from high temperatures, the trapped aluminum atoms diffuse and form some continuous and discontinuous precipitates in the α-Mg matrix and supersaturated regions, respectively. The lower aluminum content of the AM60 alloy, as compared to AZ91, results in lower driving forces for the precipitation of $Mg_{17}Al_{12}$, and thus reduces the volume fraction of these second-phase precipitates in the alloy. Although this phase increases the ambient-temperature strength of the alloy, it softens readily at temperatures above 400 K. Meanwhile, the possible formation of new precipitates leads to the consumption of Al atoms of the matrix and reduces their solid solution hardening effect. Additionally, discontinuous precipitates increase the interface area between the α-Mg and $Mg_{17}Al_{12}$, and therefore, enhance grain boundary accommodated deformation and reduce the creep resistance of the material. Similar microstructural features have been reported for other Mg-Al alloys produced via high pressure and gravity die casting methods.[19,24,25]

The microstructure of the crept specimens, depicted in Figures 10(a) and (b), shows no cavitations or crack development in the material. This could be attributed to the compressive stress state of the impression test that prevents any cavitations or crack development. The impression creep test is a localized test that measures the creep resistance of the material in small volumes. This localized nature of the test is well demonstrated in Figure 10(a), where deformation is shown to happen in a very narrow region under the indenter. Immediately beneath the indenter, there is a dead zone, where pure hydrostatic stresses prevent any deformation. Adjacent to this dead zone, shear stresses develop as a result of material's constraint, and deformation takes place. Severe deformation in this region elongates the β-$Mg_{17}Al_{12}$ particles along the deformation path. This deformation and the fracture of some of the particles, depicted in Figure 10(b), are indicative of their low efficiency in resisting the applied creep stresses. Far from the indenter, material undergoes no deformation and does not evolve during creep. In contrast to the deformation zone in AZ91, in which a pronounced discontinuous precipitation has been reported,[19] there is not a noticeable precipitation of discontinuous phase in the AM60 deformed area, probably due to the lower level of the aluminum content of the alloy.

B. Impression Creep

Impression depths plotted as a function of time under different stress levels and at various temperatures are shown in Figures 3 and 4, respectively. It can be

observed that the shape of the impression curves is similar to that of an ordinary creep curve. The first stage of the curve records an instantaneous creep strain at the beginning of the test, followed by a steady-state region, where impression depth increases linearly with time. In the steady-state creep stage, hardening mechanisms such as solid solution hardening, particle hardening, and dislocation multiplication are outweighted by different softening phenomena. These softening mechanisms include dislocation annihilation, thermal and structural instability of the low-melting point second phases, and loss of solid solution hardening at high temperatures. According to Figure 4, although the increase in the steady-state impression rate with increasing temperature from 423 to 473 K is small, this variation becomes quite significant when the temperature changes from 473 to 498 K. This could be attributed to the significant reduction in the strength of the β-$Mg_{17}Al_{12}$ phase at grain-boundary regions and the substantial work softening due to the accelerated elimination of solid-solution hardening effects at high temperatures.

The impression velocity–impression depth curves, plotted in Figure 5, indicate that there is a steep drop in the creep rates at short dwell times corresponding to the primary creep stage, followed by an almost constant impression velocity (V) region, which presumably corresponds to the steady-state creep stage of the tested materials. Since the impression test is actually a compression test, fracture of the specimen does not occur, and hence, it is obviously not possible to record an upward trend in the impression-rate curves, as opposed to that which occurs in an ordinary creep test. Figure 5 also shows that decreasing impression stress leads to a more pronounced drop in impression velocity during the primary creep stage. The observed trend is consistent with those reported for the very similar magnesium alloy, AM50.[13]

C. Identification of Rate-Controlling Mechanisms

It is generally accepted that deformation of polycrystalline materials at temperatures above $0.5 T_m$ can take place by different deformation mechanisms, associated with different stress exponents and activation energies. According to the theory of dislocation climb–controlled creep, the stress exponent has the value of 5 and the activation energy has the values of the activation energy of lattice self-diffusion.[26] At lower temperatures, dislocation pipe diffusion becomes dominant and the activation energy reaches that of the activation energy for pipe diffusion. The theory of dislocation viscous glide, however, leads to a stress exponent of 3 at high temperatures and 5 at low temperatures, the respective activation energies being equal to solute interdiffusion and to dislocation pipe diffusion.[27,28] Experimental results on the creep behavior of a series of solid solution alloys reported by Mohamed and Langdon[29] have shown that there is a transition between these two mechanisms under favorable conditions. By making assumptions concerning the nature of the climb and glide processes, they proposed a criterion for deformation by viscous glide for an Al-3 pct Mg alloy. Later, Yavari and Langdon[30]

showed that viscous glide (class A) occurs in solid solution alloys over a limited range of stresses, and there is a transition to dislocation climb (class M) at both lower and higher stress levels. In the high-stress regimes, however, there is generally a deviation from the power-law relationship. In such conditions, the stress exponents are usually greater than 6 and the creep rate increases exponentially with the applied stress.[31,32]

The stress dependence of the normalized impression velocity, shown in Figure 6, clearly indicates that in the low-stress regime, a power-law relationship with n values varying from 6.0 at low temperature to 4.2 at high temperature is valid. With increasing punching stress, however, there is an abrupt change in the stress exponent, reaching high values of 8 to 12. The stress exponents higher than 6 have been ascribed to a power-law breakdown, which is characterized by activation energies higher than that of the self-diffusion activation energy.[32] The fact that, by increasing temperature, the power-law breakdown occurs at lower stresses implies that this phenomenon is more likely to occur at higher temperatures.

Figure 7 represents the changes in the stress exponent with testing temperature. Generally, the stress exponent is an indication of the effect of stress on creep deformation. The reduction of stress exponent, in general, is due to the instability of the material microstructure at high temperatures. It has been suggested that[19] the weakening of the interdendritic β-$Mg_{17}Al_{12}$ phase, coarsening of the secondary $Mg_{17}Al_{12}$ precipitates in the supersaturated solid-solution regions, and the loss of solid solution hardening all accelerate the dislocation recovery at higher temperatures during creep. Recently, a composite model has been suggested for Mg-Al diecast alloys through which it is possible to study the effects of microstructural data, such as the concentration of solute atoms in different regions and the distribution of the secondary $Mg_{17}Al_{12}$ precipitates on the creep behavior.[33] The observed reduction of stress exponent is more pronounced in the stress regime II, where stresses are higher than those of regime I. The stronger temperature dependency of the stress exponent in region II could be justified by the higher dislocation density in this region due to higher stresses.

For the calculation of creep activation energies, the temperature dependence of the impression velocity was plotted in Figure 8. As can be seen, in the low-stress regime, the activation energies of about 84 to 76 kJ/mol are much lower than that of the self-diffusion for magnesium (Q_{sd} = 135 kJ/mole). These low activation energies are close to that for the dislocation pipe diffusion (Q_{pd}) of Mg, which can be estimated by $Q_{pd} = 0.6 \ Q_{sd}$.[34] As mentioned previously, the high-stress regime has activation energies slightly higher than Q_{sd} for magnesium. The activation energies higher than that for self-diffusion at high stresses have been also reported for Al-Cu[35] and Al-Zn[36] alloys. Considering the temperature at which creep tests were performed and stress concentration at dislocation pileups, one could conclude that the cross-slip of dislocations is a possible mechanism for dislocation movement in the present condition. It has been reported[37] that it is possible for

dislocations to cross-slip on nonbasal planes at the temperature well below what is expected. This mechanism of deformation by cross-slip depends on both stress and temperature. The relatively strong stress dependence of the activation energy in the high-stress regime, shown in Figure 9, is in accord with this mechanism.

Due to the variation in stress exponent with temperature, it was decided to offset the influence of the diffusion coefficient by normalizing the temperature-compensated impression velocity to the pipe diffusion coefficient. Thus, $VkT/D_{pd}Gb$ was plotted against σ/G on a log-log scale, as shown in Figure 11. Similar to the stress exponent and activation energy curves, the new diagram includes two distinct regimes in terms of stress. It can be depicted that the creep behavior in both low- and high-stress regimes can be expressed by two linear master curves fitted to all data obtained at different temperatures. The stress exponent for the low-stress regime is 5, which is indicative of a dislocation climb mechanism. The high correlation factor of $R^2 = 0.979$ obtained for the data after normalizing to the pipe diffusion coefficient verifies that creep in this regime is controlled by the pipe-diffusion dislocation climb. The transition from the low-stress to the high-stress regime occurs at $\sigma/G \approx 0.03$, above which the stress exponent of 10.1 is obtained. The slight scatter of the data obtained at different temperatures in the high-stress regime has resulted in a lower correlation factor of $R^2 = 0.823$. This may be attributed, in part, to the change in the microstructure during the impression creep at different temperatures. Furthermore, in the power-law breakdown regime, the creep behavior is mostly expressed by an exponential relationship rather than a linear one. The main purpose of fitting a straight line to the high-stress regime data is thus to show the higher values of the stress exponent, as compared to those obtained in the low-stress regime obeying a power-law relationship.
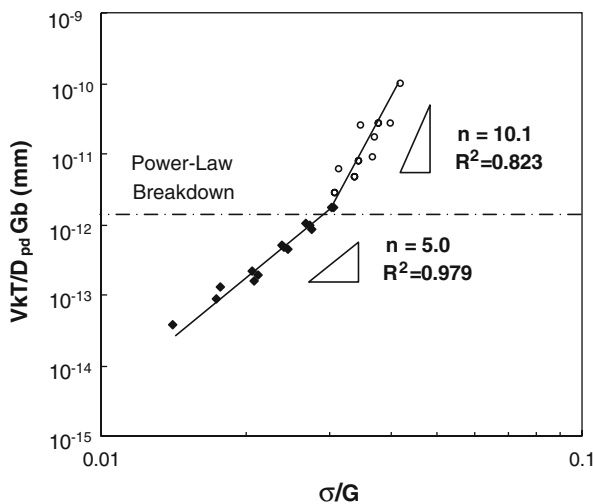
According to the empirical relationship proposed by Sherby and Burke,[32] the transition from power law to exponential relationship occurs at $\frac{\dot{\varepsilon}}{D} = 10^{13}$ m^{-2}. The results shown in Figure 11 indicate that the power law breaks down at $\frac{VkT}{D_{pd}Gb} = 2 \times 10^{-12}$ mm, which is equivalent to $\frac{\dot{\varepsilon}}{D} = 7 \times 10^8$ m^{-2}, when proper values are assigned to G, b, k, and T. This is well below the $\frac{\dot{\varepsilon}}{D} = 10^{13}$ m^{-2} predicted from the criteria proposed by Sherby and Burke.[32] The observed difference is probably due to the fact that they have considered materials the deformation mechanism of which is controlled by lattice diffusion, while the dislocation climb in the present work is controlled by pipe diffusion. Similar disagreements between experimental and predicted values have been reported for polycrystalline copper.[38]

V. CONCLUSIONS

Impression creep characteristics of the AM60 magnesium alloy investigated in the temperature range 423 to 523 K under different stress levels yielded the following conclusions.

1. The creep resistance of the AM60 alloy was adversely affected by the low thermal stability and low strength of the β-Mg$_{17}$Al$_{12}$ intermetallic phase dispersed in the α-Mg matrix. No discontinuous precipitation of the lamellar β-Mg$_{17}$Al$_{12}$ phase was observed in the stressed area under the indenter.
2. Depending on the punch stress, the creep behavior was divided into two stress regimes, with a change from the low-stress regime to the high-stress regime occurring at around $\sigma/G = 0.03$. The obtained strain exponents, which decreased with increasing temperature, were found to be 4 to 6 and 8 to 12 for the low- and high-stress regimes, respectively. These values changed to 5 and 10.1 when the experimental creep rates were normalized to the pipe-diffusion coefficient.
3. Analogous to the stress exponent trend, there were two distinct regimes for the activation energy of creep deformation. In both regimes, the activation energy decreased as the stress increased. The low-stress regime activation energies of about 76 to 84 kJ mol^{-1}, which are close to 80 kJ mol^{-1} for dislocation-pipe diffusion in the Mg, and the stress exponent of 5 imply that the operative creep mechanism is pipe-diffusion-controlled dislocation climb. In the high-stress regime, there exists a power-law breakdown with the activation energy values of about 134 to 165 kJ mol^{-1}. These activation energies together with the stress exponent of 10 are indicative of a dislocation creep mechanism.

Fig. 11—(a) Temperature-compensated impression velocity normalized to the pipe diffusion coefficient (D_{pd}), Burgers vector (b), and shear modulus (G), where all data emerge into one master line for each stress regime.

REFERENCES

1. C. Blawert, N. Hort, and K.U. Kainer: *Trans. Indian Inst. Met.*, 2004, vol. 57, pp. 397–408.
2. B.L. Mordike and T. Ebert: *Mater. Sci. Eng.*, 2001, vol. A302, pp. 37–45.

3. S.S. Vagarali and T.G. Langdon: *Acta Metall.*, 1981, vol. 29, pp. 1969–82.
4. W. Blum, Y.J. Li, X.H. Zeng, P. Zhang, B. Von Grobmann, and C. Haberling: *Metall. Mater. Trans. A*, 2005, vol. 36A, pp. 1721–28.
5. M. Wang, H. Zhou, and L. Wang: *J. Rare Earths*, 2007, vol. 25, pp. 233–37.
6. M. Vogel, O. Kraft, and E. Arzt: *Metall. Mater. Trans. A*, 2005, vol. 36A, pp. 1713–19.
7. A. Srinivasan, J. Swaminathan, U.T.S. Pillai, K. Guguloth, and B.C. Pai: *Mater. Sci. Eng.*, 2008, vol. A485, pp. 86–91.
8. A.A. Luo, B.R. Powell, and M.P. Balogh: *Metall. Mater. Trans. A*, 2002, vol. 33A, pp. 567–74.
9. P. Zhang: *Scripta Mater.*, 2005, vol. 52, pp. 277–82.
10. W. Blum, P. Eisenlohr, and F. Breutinger: *Metall. Mater. Trans. A*, 2002, vol. 33A, pp. 291–303.
11. K.U. Kainer: *Magnesium Alloys and Technology*, Wiley-VCH Verlag GmbH & Co. KG aA, Weinheim, 2003, pp. 1–23.
12. W. Blum, P. Zhang, B. Watzinger, B.V. Grossmann, and H.G. Haldenwanger: *Mater. Sci. Eng.*, 2001, vols. A319–A321, pp. 735–40.
13. N. Ishimatsu, Y. Terada, T. Sato, and K. Ohori: *Metall. Mater. Trans. A*, 2006, vol. 37A, pp. 243–48.
14. S.N.G. Chu and J.C.M. Li: *J. Mater. Sci.*, 1977, vol. 12, pp. 2200–08.
15. H. Deming, C. Yungui, T. Yongbai, L. Hongmei, and N. Gao: *Mater. Lett.*, 2007, vol. 61, pp. 1015–19.
16. H. Liu, Y. Chen, Y. Tang, S. Wei, and G. Niu: *Mater. Sci. Eng.*, 2007, vol. A464, pp. 124–28.
17. H. Liu, Y. Chen, Y. Tang, S. Wei, and G. Niu: *J. Alloys Compd.*, 2007, vol. 440, pp. 122–26.
18. L. Peng, F. Yang, J.F. Nie, and J.C.M. Li: *Mater. Sci. Eng.*, 2005, vols. A410–411, pp. 42–47.
19. F. Kabirian and R. Mahmudi: *Metall. Mater. Trans. A*, 2009, vol. 40A, pp. 116–27.
20. A.K. Mukherjee, J.E. Bird, and J.E. Dorn: *Trans. ASM*, 1969, vol. 62, pp. 155–79.
21. A. Juhasz, P. Tasnadi, P. Szasvari, and I. Kovacs: *J. Mater. Sci.*, 1986, vol. 21, pp. 3287–91.
22. R. Mahmudi, R. Roumina, and B. Raeisinia: *Mater. Sci. Eng.*, 2004, vol. A382, pp. 15–22.
23. K. Ishikawa, H. Watanabe, and T. Mukai: *Mater. Lett.*, 2005, vol. 59, pp. 1511–15.
24. D. Wenwen, S. Yangshan, M. Xuegang, X. Feng, Z. Min, and W. Dengyun: *Mater. Sci. Eng.*, 2005, vol. A356, pp. 1–7.
25. P. Zhang, B. Watzinger, and W. Blum: *Phys. Status Solidi A*, 1999, vol. 175, pp. 481–87.
26. M.D. Mathew, H. Yang, S. Movva, and K.L. Murty: *Metall. Mater. Trans. A*, 2005, vol. 36A, pp. 99–105.
27. T. Reinikainen and J. Kivilahti: *Metall. Mater. Trans. A*, 1999, vol. 30A, pp. 123–32.
28. R. Mahmudi, A. Rezaee-Bazzaz, and H.R. Banaie-Fard: *J. Alloy. Compd.*, 2007, vol. 429, pp. 192–97.
29. F.A. Mohamed and T.G. Langdon: *Acta Metall.*, 1974, vol. 22, pp. 779–88.
30. P. Yavari and T.G. Langdon: *Acta Metall.*, 1982, vol. 30, pp. 2181–96.
31. S.V. Raj: *Mater. Sci. Eng.*, 2002, vol. A322, pp. 132–47.
32. O. D. Sherby and P.M. Burke: *Prog. Mater. Sci.*, 1968, vol. 13, pp. 325–90.
33. S. Spigarelli: *Mater. Sci. Eng.*, 2008, vol. A492, pp. 153–60.
34. J.P. Poirier: *Creep of Crystals, High Temperature Deformation Processes in Metals. Ceramics and Minerals*, Cambridge University Press, New York, NY, 1985.
35. P.K. Chaudhury and F.A. Mohamed: *Metall. Trans. A*, 1987, vol. 18A, pp. 2105–14.
36. M.S. Soliman and F.A. Mohamed: *Metall. Trans. A*, 1984, vol. 15A, pp. 1893–1904.
37. M. Regev, A. Rosen, and M. Bamberger: *Metall. Mater. Trans. A*, 2001, vol. 32A, pp. 1335–45.
38. S.V. Raj and T.G Langdon: *Acta Metall.*, 1989, vol. 37, pp. 843–52.